International Journal of Heat and Mass Transfer 164 (2021) 120526

Contents lists available at ScienceDirect

International Journal of Heat and Mass Transfer

journal homepage: www.elsevier.com/locate/hmt

Deposit geometry and oxygen concentration spatial variations due to composition change in printed functionally graded components

J.S. Zuback[a], G.L. Knapp[a,*], T.A. Palmer[a,b], T. DebRoy[a]

[a] Department of Materials Science and Engineering, The Pennsylvania State University, University Park, 16802, PA
[b] Department of Engineering Science and Mechanics, The Pennsylvania State University, University Park, 16802, PA

ARTICLE INFO

Article history:
Received 15 July 2020
Revised 21 September 2020
Accepted 22 September 2020
Available online 10 October 2020

Keywords:
Additive manufacturing
Directed energy deposition
Functionally graded materials
Surface-active elements
Marangoni convection

ABSTRACT

Functionally graded materials (FGMs) with site specific chemical composition are commonly manufactured by directed energy deposition (DED). Although previous work fabricated an FGM with a compositional variation between a ferritic and austenitic alloy, difficulties arose due to variations in deposit shape with composition change. This problem also occurs for FGMs in literature; however, unlike other cases, the thermophysical properties of these two alloys were similar throughout the build. Here, we investigate the role of chemical composition and surface-active elements on deposit geometry during the manufacture of FGMs by laser DED. Single-track experiments for the relevant FGM compositions are analyzed with results from a well-tested, three-dimensional, transient numerical heat transfer and fluid flow model and thermodynamic calculations. Experiments showed deposit shape varied as a function of composition for constant laser power and scan speed. Thermodynamic analysis indicated that the oxygen solubility in the fusion zone varied significantly for each composition used for the FGM. Numerical modeling revealed that the change in fluid flow caused by Marangoni convection due to dissolved oxygen in the fusion zone were mainly responsible for the changes in deposit shape observed in experiments. Because oxygen can be introduced into the fusion zone through the feedstock as well as the surrounding atmosphere, these findings elucidate a previously unconsidered aspect of process control during DED fabrication of FGMs.

1. Introduction

Additive manufacturing allows the printing of unique metallic parts with site-specific chemical composition and properties [1–3]. This design, known as functionally graded material (FGM), cannot be easily made by conventional manufacturing. Their functionality is attracting many applications. For example, an FGM could prevent creep failure of dissimilar metal joints between a ferritic and an austenitic alloy by slowing down the diffusive migration of carbon [4]. Directed energy deposition (DED) is commonly used for the manufacturing of FGMs, where the chemical composition of each layer gradually changes along the build direction. The utility of FGMs is well recognized, but their manufacturing and qualification require close attention to process planning, process control, and most importantly, defect mitigation.

Achieving superior properties and serviceability requires the selection of appropriate process parameters [5, 6], often following machine manufacturers' recommendations, and increasingly using machine learning [7]. After an AM build begins, the sensing and control hardware and software perform two main tasks, control part geometry and reduce defects. Sensing often involves measurement of fusion zone attributes because the fusion zone geometry and temperature distribution affect the defects, microstructures, and properties [8]. Therefore, it is important to understand the factors that influence the fusion zone attributes of FGMs.

Several factors influence fusion zone geometry and temperature profiles [9, 10]. The first factor is thermal diffusivity, which depends on thermal conductivity, density, and specific heat of the material and affects the conduction of heat in the build. Thermal diffusivity typically varies along the build direction in FGMs because of the changes in the alloy composition and thermophysical properties. This variation may affect the fusion zone geometry and temperature profiles even when the laser power and scanning speed are kept constant. Secondly, heat is transported by convection within the fusion zone. The liquid metal undergoes vigorous recirculatory flow within the melt pool owing to the Marangoni effect [9, 10]. Because of the spatial variation of temperature from the middle of the melt pool to its periphery, a spatial gradient of interfacial tension, known as Marangoni stress, is established. This stress is a powerful driver of convective flow. Convective heat transfer is often the dominant mechanism of heat flow within the

* Corresponding author.
E-mail address: glk9@psu.edu (G.L. Knapp).

https://doi.org/10.1016/j.ijheatmasstransfer.2020.120526
0017-9310/

Table 1
Chemical composition (in wt%) of materials as provided by the manufacturers. The compositions of the baseplate, Pyromet® 800 (i.e., 800H) and Fe powder are balanced with Fe, and single values in the baseplate composition represent maximum allowable concentration.

Material	Al	Cr	Mn	Ni	Si	Ti	C	O	S	Other
Baseplate	-	2.0-2.5	0.3-0.6	-	0.50	-	0.05-0.15	0.035	0.035	0.035P, 0.90-1.1Mo
Pyromet® 800	0.38	21.0	0.88	34.0	0.62	0.41	0.095	0.015	0.006	0.003P, 0.003N
Fe Powder	0.002	0.002	-	0.03	-	-	0.003	0.01	-	0.007Co
Cr Powder	0.02	Bal.	-	-	0.01	-	0.02	0.02	0.01	0.02Fe

fusion zone and it affects the geometry of the fusion zone and the temperature profiles in the entire component [9, 10].

The convection pattern in the melt pool is significantly influenced by the direction of the Marangoni stress [11–14]. In most alloys, the interfacial tension decreases with the increase in temperature, and the liquid metal flows from the middle of the melt pool to its periphery resulting in a wide and shallow melt pool [11–13]. However, the flow pattern changes dramatically when surface-active elements, i.e., the alloying elements that have large negative enthalpies of segregation such as oxygen and sulfur are present in the melt [14]. In melts containing these elements, the convective flow pattern reverses and the liquid metal flows from the periphery to the middle and then goes downward. As a result, the fusion zone tends to be relatively narrow and deep [11–14]. Similar observations have been made in laser based DED processing of a range of alloy systems containing sulfur, including Co-based [15], Ti-6Al-4V [16] and Inconel 718 [17] alloys. Though most DED processes are carried out in an inert gas chamber with atmospheric oxygen on the order of 10 parts per million (ppm) [18], oxygen and sulfur exist in the powder feedstock and can increase if powder is reused [19]. Elmer et al. [20] recently showed that a significant amount of oxygen can dissolve in alloys from the environment during AM when no purge gas was used during wire arc additive manufacturing, showing the importance of atmospheric control.

Since the local alloy composition varies in different layers in FGMs, the oxygen solubility also varies with composition. Both the alloy composition and the oxygen concentration may change in different layers along the build direction. While the effects of surface-active elements have been studied widely in the welding literature [11–14], the consequences of these effects combined with changing composition are presently unstudied for the fabrication of FGMs. Because surface-active elements change the shape of the molten pool, the spatial variation of oxygen solubility along the build direction has the potential to affect the production of FGMs profoundly. Significant changes in the fusion zone shape and size can lead to lack of fusion defects [5, 21] and deviations of the final part geometry from the target value. A better understanding of the composition-dependent, layer-wise variations of oxygen concentrations and the associated effects are needed to achieve sound understanding of the production of FGMs by DED and improve process control. Furthermore, no data or analysis of the role of oxygen in the production of FGMs are presently available in the additive manufacturing literature.

Here, for the first time, we present data and analysis about the role of oxygen in the manufacture of FGMs by DED-L. This work builds off previous work of a fabrication of an FGM of ferritic alloy 2.25Cr-1Mo steel to austenitic alloy Alloy 800H [4]. Single-layer, single-pass deposits are made of each composition in the FGM to isolate the effects of composition on the deposit shape. The effects of oxygen solubility in the molten pool are explained through thermodynamic analysis of oxygen activity for each composition in the FGM combined with both characterization of the experiments and a well-tested numerical model. Uniquely, the numerical model considers the temperature dependence of surface tension considering sulfur and oxygen activity in the alloy. Overall, this investigation details the effect of surface-active elements during the processing of FGM by DED, which will benefit the design and process control of FGMs.

2. Methods

2.1. Experiments

Commercially pure Fe and Cr powders (Atlantic Equipment Engineers, Micron Metals, Inc.) were mixed with pre-alloyed Micro-Melt® Pyromet 800 powder (Carpenter Powder Products), hereafter referred to as “800H”, to replicate the compositional grading achieved in the fabrication of previous functionally graded structures [4]. All powders had a size range between 45 and 145 μm in diameter, and the compositions are listed in Table 1. Powder mixtures ranging from 10 to 60% 800H, by weight, were deposited onto a 150 mm x 150 mm x 12.7 mm normalized and tempered SAE387 Grade 22 steel substrate (American Alloy Steel) in an Ar gas environment using a laser based DED process. A partial gradient from 10 to 60% 800H was used for the analysis because a full composition gradient from 10 to 100% 800H was previously deemed unnecessary for the FGM to fulfill its designed functionality. Prior to deposition, the steel substrate was ground to remove the oxide scale and cleaned with acetone. A scanning speed of 10.6 mm/s, powder flow rate of 15 g/min, and 4 mm laser beam diameter were held constant for all deposits. A schematic diagram of the FGM between 2.25Cr-1Mo steel and Alloy 800H on which these deposits are based is shown in Fig. 1(a). Fig. 1(b) shows the designed concentration profile, showing the stepwise variation in composition and indicating that single-track depositions of each region will display similar behavior. Additional details on the experimental setup can be found in related work [4, 22, 23].

Metallographic cross sections approximately 3 mm thick were extracted perpendicular to the scanning direction using an abrasive saw at a location near the middle of each deposit. The samples were mounted in epoxy and ground with a series of silicon carbide papers up to P2000 ISO grit size to remove damage from sectioning. A mirror finish was obtained by polishing with 3 and 1 μm diamond suspensions followed by a final polishing step with 0.05 μm colloidal silica. Micrographs of the transverse cross sections were acquired using an optical microscope. All measurements and image analysis of metallurgical cross-sections were performed using ImageJ [24]. The remaining portions of the deposit were analyzed by optical profilometry measurements using a Keyence VHX-2000 digital optical microscope to obtain width and height measurements along the length of the deposit.

Fig. 2 shows a schematic illustration of the locations where measurements were made of the size of the cross section in both the experiments and model results. The dilution depth, d, is defined as the maximum penetration into the substrate measured from the original location of the top of the substrate. The deposit width, w, represents the length between the two contact points of the bead on the substrate surface. The melted area below the substrate, A_d, and the area of the deposited bead material, A_b, are used

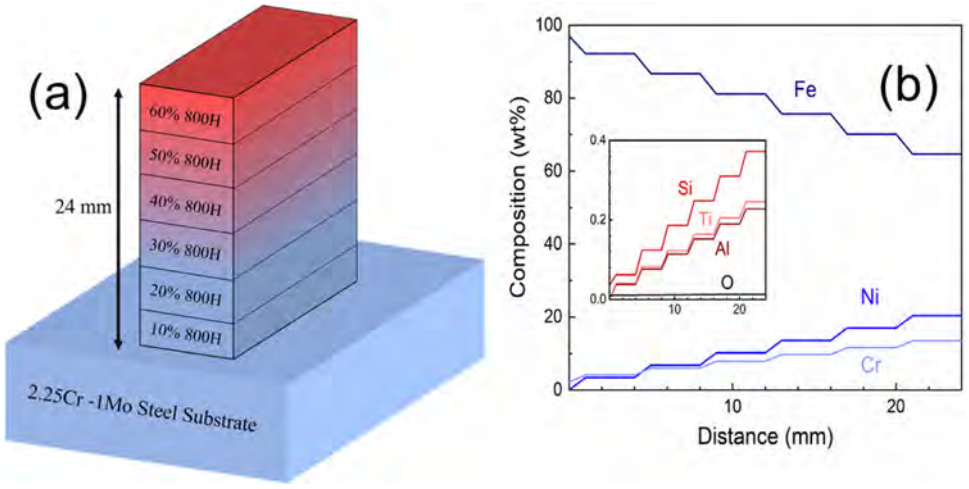

Fig. 1. (a) A schematic diagram of the functionally graded material between 2.25Cr-1Mo steel and Alloy 800H. (b) Designed concentration profiles of Fe, Ni, Cr, Si, Ti and Al along the build direction.

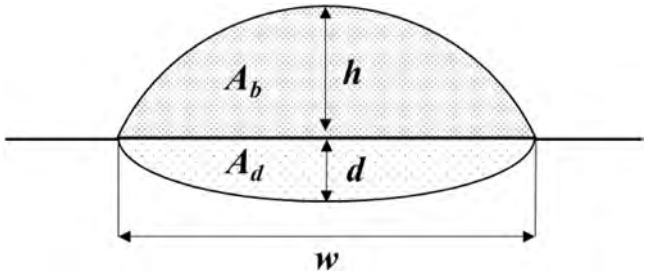

Fig. 2. Schematic of a deposit with the dilution area (A_d), bead area (A_b), bead height (h), and dilution depth (d) labeled.

to define the percentage of dilution as,

$$D = \frac{A_d}{A_b + A_d} \times 100 \tag{1}$$

2.2. Modeling

To evaluate the effects of alloy composition on molten pool geometry, equilibrium thermodynamic calculations are used to determine the activity of surface-active elements and to estimate thermophysical properties for each alloy composition. Various software packages with their accompanying databases use the CALPHAD method [25] to calculate phase equilibria and thermodynamic parameters in multi-component alloys. In this work, JMatPro® V8 [26] was used with the General Steel database to calculate oxygen and sulfur activities and the accompanying thermophysical properties for the alloy compositions which comprise this FGM. The calculations of surface tension containing surface active elements are described in the Appendix and the corresponding thermophysical properties used for numerical simulations are shown in Table 2 [26].

Calculated thermophysical properties are then used in a numerical heat transfer and fluid flow model to determine the 3D temperature and velocity fields and molten pool geometries for each alloy composition. The heat transfer and fluid flow model solves the governing equations for conservation of mass, momentum, and energy, respectively defined as [27],

$$\frac{\partial(\rho u_i)}{\partial x_i} = 0, \tag{2}$$

$$\frac{\partial(\rho u_j)}{\partial t} + \frac{\partial(\rho u_j u_i)}{\partial x_i} = \frac{\partial}{\partial x_i}\left(\mu \frac{\partial u_j}{\partial x_i}\right) + S_j \tag{3}$$

$$\rho \frac{\partial h}{\partial t} + \frac{\partial(\rho u_i h)}{\partial x_i} = \frac{\partial}{\partial x_i}\left(\frac{k}{C_p}\frac{\partial h}{\partial x_i}\right) - \rho \frac{\partial \Delta H}{\partial t} - \rho \frac{\partial(u_i \Delta H)}{\partial x_i} + S_V \tag{4}$$

Here, ρ is the density, x_i is the spatial position on the i-axis ($i = 1, 2, 3$, corresponding to Cartesian x, y, z), u_i and u_j are velocities in the i and j directions ($j = 1, 2, 3$), t is time, μ is the dynamic viscosity, h is specific effective heat, C_p is specific heat, and ΔH is the latent heat content. The volumetric source term for the momentum equation in the j-direction is S_j, which is defined by the Marangoni stress on the surface [27]. The volumetric term for the energy equation S_V is defined by the heat input from the Gaussian-distributed heat source [27], heat loss from radiation and natural convection at the free surface [27], forced convection due to gas flow [28], and vaporization heat loss at the free surface [29].

The domain consists of cells with either alloy or gaseous properties. Temperature-dependent material properties for the alloys are listed in Table 2 and the gas properties for the energy equation are approximate values for argon ($k = 2.6e-3\ J\ m^{-1}\ K^{-1}$, $C_p = 520\ J\ kg^{-1}\ K^{-1}$, $\rho = 0.974\ kg\ m^{-3}$) [30]. Solid material and gas are considered stationary for the solution of the mass and momentum governing equations. Boundary conditions for the at the edge of the domain are natural convection ($h_c = 8.4\ J\ m^{-2}\ s^{-1}\ K^{-1}$) and radiation to ambient temperature (298 K).

The details of the discretization using the finite difference method and solution using the semi-implicit method for pressure-linked equations are described by Patankar [31] and others [27, 32]. Convection is the dominant mechanism of heat transfer in AM [9, 10] and is driven by the spatial gradient of surface tension. In the absence of surface-active elements, such as oxygen and sulfur, the temperature coefficient of surface tension is typically a negative constant, meaning liquid metal will flow outwards from regions of high to low temperatures. However, the presence of surface-active elements can cause inward liquid metal flow resulting from the depression of surface tension at temperatures slightly above the liquidus temperature. A theoretical description of the surface tension of molten alloys with surface-active elements has been developed for calculating surface tension in binary [14] and ternary [33] alloys, and it is described in Appendix A.2. Using this

Table 2
Thermophysical material properties for each alloy composition used in numerical calculations [26].

Property	Units	Material Substrate	10% 800H	20% 800H	30% 800H	40% 800H	50% 800H	60% 800H
Solidus temperature, T_s	K	1739	1746	1736	1707	1689	1671	1650
Liquidus temperature, T_l	K	1787	1770	1759	1747	1737	1727	1714
Specific heat of solid, $c_{p,s}$	$J\ kg^{-1}\ K^{-1}$	420+0.167T	420+0.167T	420+0.167T	331+0.251T	331+0.251T	331+0.251T	331+0.251T
Specific heat of liquid, $c_{p,l}$	$J\ kg^{-1}\ K^{-1}$	810	800	800	790	790	790	780
Thermal conductivity of solid, k_s	$J\ m^{-1}\ K^{-1}$	13.6+0.0126T	12.3+0.0126T	11.2+0.0126T	10.2+0.0126T	9.54+0.0126T	9.04+0.0126T	8.66+0.0126T
Thermal conductivity of liquid, k_l	$W\ m^{-1}\ K^{-1}$	32.7	32.33	32.1	31.7	31.5	31.2	30.86
Density, ρ	$kg\ m^{-3}$	7830	7840	7890	7940	7970	7940	7920
Surface tension at T_l, σ	$N\ m^{-1}$	1.838	1.805	1.785	1.751	1.738	1.727	1.719
Temperature-coefficient of surface tension, $d\sigma/dT$	$N\ m^{-1}K^{-1}$	-4.44×10^{-4}	-3.84×10^{-4}	-3.52×10^{-4}	-3.50×10^{-4}	-3.33×10^{-4}	-3.17×10^{-4}	-3.03×10^{-4}
Latent heat of fusion, ΔH	$J\ kg^{-1}$	2.62×10^5	2.58×10^5	2.51×10^5	2.56×10^5	2.57×10^5	2.56×10^5	2.59×10^5
Liquid viscosity, μ	$kg\ m^{-1}s^{-1}$	6.67×10^{-3}	6.81×10^{-3}	6.89×10^{-3}	6.97×10^{-3}	7.03×10^{-3}	7.09×10^{-3}	7.21×10^{-3}
Thermal expansion coefficient, α	K^{-1}	1.78×10^{-6}	1.78×10^{-6}	1.96×10^{-6}	2.16×10^{-6}	2.31×10^{-6}	2.26×10^{-6}	2.22×10^{-6}
Absorption coefficient at 1064 nm wavelength, η	-	0.351	0.344	0.337	0.329	0.322	0.315	0.308
Emissivity, ε	-	0.3	0.3	0.3	0.3	0.3	0.3	0.3

method, the surface tension of each alloy was be calculated as a function of temperature for each composition.

The free surface profile of each deposit is calculated by coupling the transient heat transfer and fluid flow model to a surface energy minimization model, which is based on a method originally developed for simulation of arc welding [34, 35]. An iterative procedure was used to solve for the three-dimensional velocity components, sensible heat, and pressure at each time step. After the time step is converged, the deformation of the current surface, ϕ, is calculated by solving the equation governing the energy needed to deform the free surface of the molten pool using the method of Lagrangian multipliers with the Gauss-Seidel method [35],

$$\gamma\left(\frac{\left(1+\phi_y^2\right)\phi_{xx}-2\phi_x\phi_y\phi_{xy}+\left(1+\phi_x^2\right)\phi_{yy}}{\left(1+\phi_x^2+\phi_y^2\right)^{3/2}}\right)=\rho g\phi+P_a+\lambda \quad (5)$$

under the constraint,

$$\int_A \phi dA-\dot{V}\Delta t=0 \quad (6)$$

The Lagrangian multiplier is λ, external pressure acting on the surface is P_a ($P_a=-2\gamma\kappa$ by Young-Laplace equation), and g is acceleration due to gravity. The constraint provides that the total volume added by deforming the surface area, A, by distance ϕ is equal to the volume added in the time step, $\dot{V}\Delta t$. The volume added is calculated based on the ratio of area of the powder stream (equal to the laser beam diameter) incident on the molten pool over the area of the entire powder stream [36, 37]. Material with temperature $T < T_S$ does not deform. Once the surface deformation is solved, any control volumes newly enclosed by the surface are updated to have properties of the deposited material. The next time step is then executed, temperature and velocity fields converged, the free surface calculated again, etc. Further details of the free surface calculations are available in the literature [34, 35].

3. Results and discussion

3.1. Variations in chemical composition and bead geometry

Changes in alloy composition and laser power have noticeable impacts on the size and shape of the as-deposited pool geometry. In the case of changes in composition, as shown in Fig. 3, increases in the amount of 800H in the powder feedstock produce changes in both the deposit width and depth. Based on the measurements of total melted area ($A_b + A_d$) and the size of the dilution region with changes in laser power, which are shown in Table 3, increasing laser power causes an increase in the overall dimensions of the deposit regardless of composition. On the other hand, increases in the amount of 800H added to the powder feedstock produced no consistent trend in the total melted area, indicating that changes in laser power are responsible for the total volume of the molten pool, while changes in composition impact the shape.

In addition to changes in the size and shape of the deposit, changes in chemical composition have an impact on the amount of substrate melted or dilution depth. For all laser powers, the 10% 800H case had the deepest dilution depth, as shown in Table 3. The bottom edge of the fusion zone that penetrates the substrate also varies in shape as the 800H alloy content increases. For example, with an addition of 10 % 800H, the fusion zone boundary is semi-circular, and it becomes flatter and shallower as more 800H is added. Since the thermophysical properties of the alloys in Table 1 are similar, these changes in pool shape cannot be directly attributed to differences in material properties, as will be discussed further in Section 3.3.

Since changes in the deposit shape below the substrate surface can complicate the measurements of the deposit height and width,

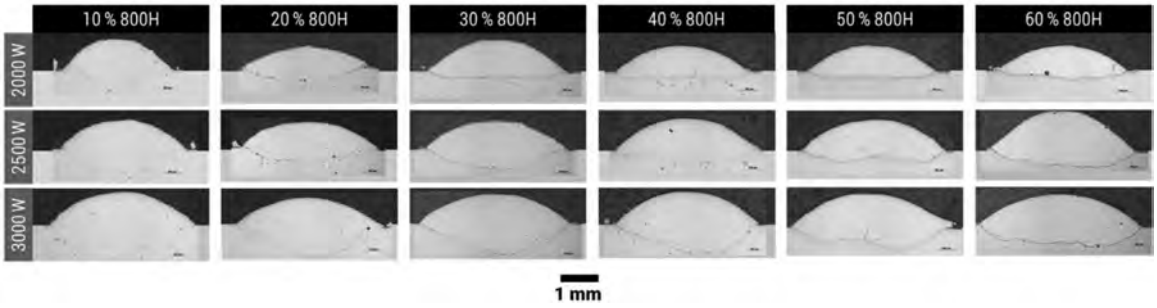

Fig. 3. Transverse cross-sections of the deposits obtained during experiments. Bead shape can be seen to change as a function of composition and laser power (% 800H labelled on each column, total laser power labelled on each row). All images share the same scale, indicated by the scale bar at the bottom of the figure.

Table 3
Measurements obtained from metallographic cross sections of single bead deposits for different material compositions and laser powers. Errors from bead area are estimated from error in width and height and error for dilution error is taken as the same percent error as the corresponding bead area. Error is propagated to total melted area and dilution. Dilution depth error is equivalent to the corresponding height error in percentage error.

Measurement	Units	Laser power [W]	Material 10% 800H	20% 800H	30% 800H	40% 800H	50% 800H	60% 800H
		2000	1.61±0.3	1.43±0.4	2.07±0.2	1.62±0.4	1.59±0.2	1.59±0.3
Bead area (A_b)	[mm^2]	2500	1.79±0.2	1.95±0.2	2.05±0.3	2.15±0.2	2.10±0.2	2.84±0.3
		3000	2.14±0.3	1.94±0.3	2.19±0.5	2.36±0.3	2.66±0.2	2.40±0.3
		2000	0.38±0.1	0.62±0.2	0.42±0.1	0.53±0.1	0.50±0.1	0.54±0.1
Dilution area (A_d)	[mm^2]	2500	1.13±0.1	0.76±0.1	1.18±0.2	0.75±0.1	0.73±0.1	1.15±0.1
		3000	1.98±0.2	1.75±0.3	1.93±0.4	1.84±0.2	1.41±0.1	1.74±0.2
		2000	1.99±0.4	2.05±0.6	2.50±0.3	2.14±0.3	2.09±0.3	2.13±0.4
Total melted area ($A_b + A_d$)	[mm^2]	2500	2.92±0.3	2.71±0.3	3.23±0.5	2.90±0.2	2.83±0.3	3.99±0.4
		3000	4.11±0.5	3.68±0.6	4.11±0.9	4.20±0.5	4.07±0.3	4.14±0.5
		2000	13 - 27	19 - 44	12 - 22	18 - 34	18 - 30	19 - 33
Dilution	[%]	2500	34 - 44	23 - 33	29 - 44	22 - 30	22 - 30	25 - 33
		3000	42 - 54	39 - 56	36 - 59	38 - 50	31 - 38	36 - 48
		2000	0.27±0.03	0.25±0.02	0.13±0.01	0.14±0.02	0.18±0.01	0.24±0.03
Dilution depth (d)	[mm]	2500	0.58±0.03	0.34±0.01	0.49±0.02	0.28±0.01	0.26±0.01	0.39±0.01
		3000	0.87±0.04	0.79±0.04	0.80±0.06	0.72±0.04	0.56±0.01	0.54±0.01

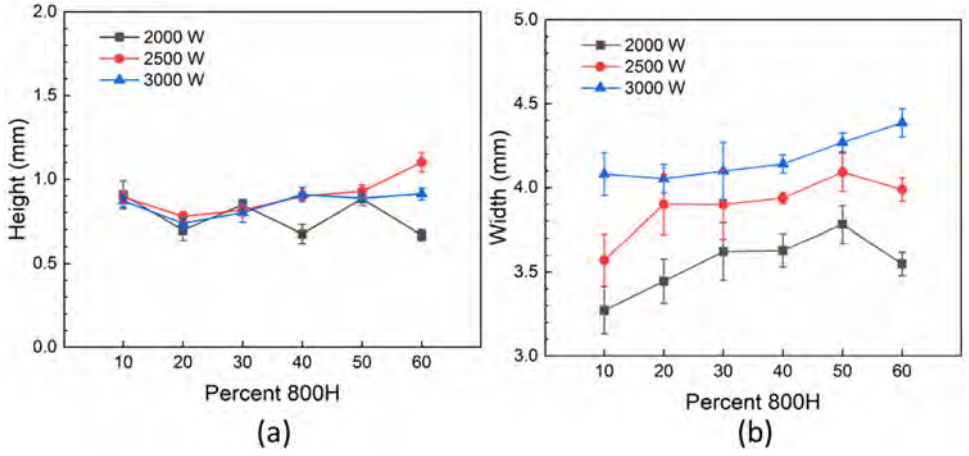

Fig. 4. The effects of laser power and alloy composition on the (a) height and (b) width of single pass, single layer deposits.

optical profilometry measurements across the length of the deposit were made and are summarized in Fig. 4 (a) and (b), respectively. As shown in Fig. 4 (a), only small deviations in bead height were observed with changes in the alloy composition, while laser power did not have any discernible impact. On the other hand, the deposit width exhibits a general upward trend with increasing 800H additions at each laser power, as shown in Fig. 4 (b). Increases in laser power also produce wider deposits for all compositions.

3.2. Effects of composition on surface tension

In welding and AM processes, the addition of surface-active elements, such as oxygen and sulfur, is known to influence the molten pool shape by altering Marangoni flow through changes in the temperature-dependent surface tension (γ) [11, 38]. Through calculations of the activity of both oxygen and sulfur across the range of FGM compositions, as described in the Appendix, important connections between composition, surface tension, and the geometry of the deposit were identified. As a baseline for calculations to follow, the changes in the oxygen and sulfur activities across a range of different oxygen and sulfur concentrations are shown in Fig. 5 (a) and (b), respectively. Significant differences in the oxygen and sulfur activities are evident with changes in both the overall FGM compositions and with increasing oxygen and sulfur concentrations. For example, the calculated oxygen activities can be one to two orders of magnitude lower than the total oxy-

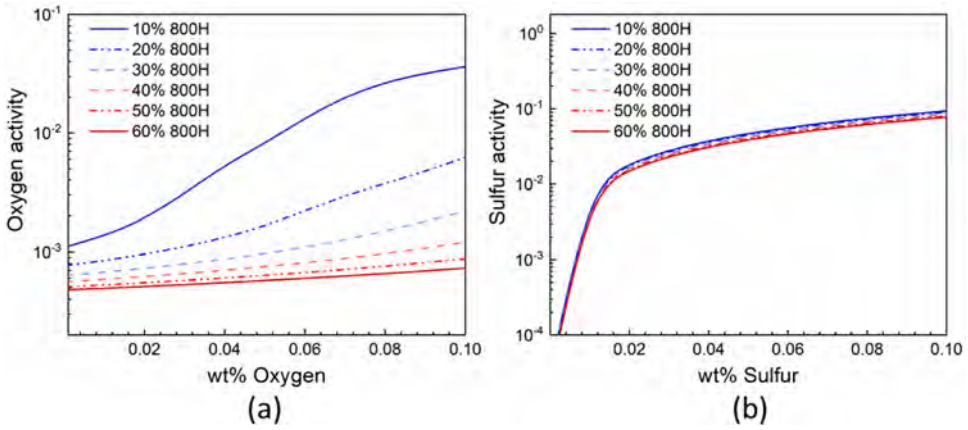

Fig. 5. The thermodynamic activities of (a) oxygen and (b) sulfur as a function of total alloy concentration in the liquid alloy at 1600°C.

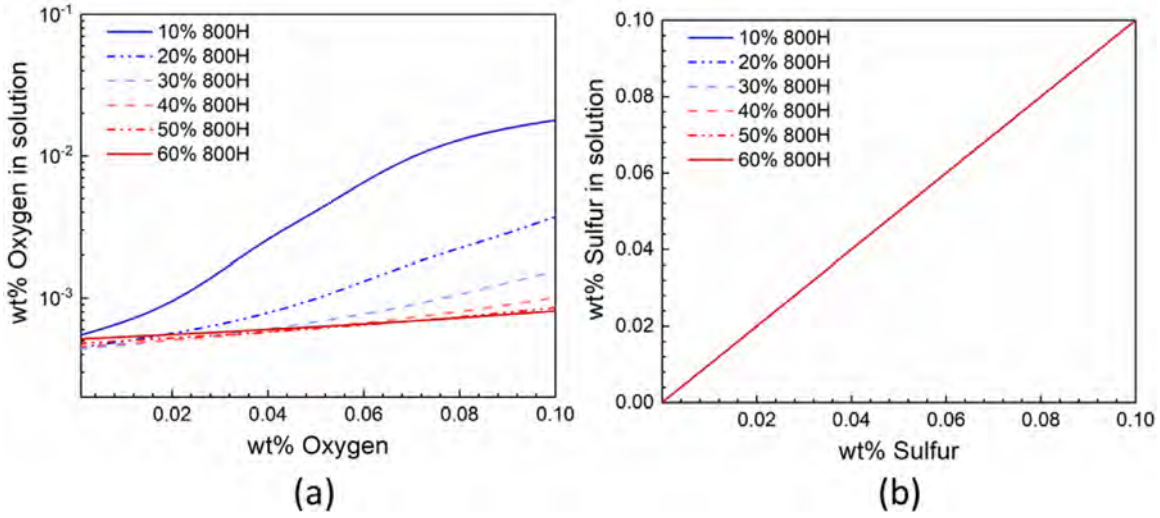

Fig. 6. The equilibrium concentrations of (a) oxygen and (b) sulfur in solution as a function of total alloy concentration in the liquid alloy at 1600°C.

gen concentration, particularly with higher levels of 800H. Similar trends are observed with changes in the amount of 800H added to the FGM, with increases in the 800H levels from 10% to 60% resulting in a decrease in calculated oxygen activity of nearly two orders of magnitude. On the other hand, the calculated sulfur activities are much less sensitive to changes in the 800H additions and differ by negligible amounts across the range from 10 to 60% 800H.

The differences in the response of the calculated oxygen and sulfur activities to changes in alloy composition are largely due to interactions between alloying elements. In these alloys, changes in minor alloying element concentrations can affect the amounts of surface-active elements that remain in solution in the liquid alloy. For example, the equilibrium solubilities of oxygen and sulfur in the liquid phase at 1600°C are shown in Fig. 6 (a) and (b), respectively. In contrast to the sulfur concentration, which does not change with changes in the FGM composition, the oxygen solubility is highly dependent on alloy composition, particularly at lower 800H levels. Since Alloy 800H contains deoxidizing elements, such as Al, Si, and Ti, the amount of oxygen in the liquid solution decreases as oxide inclusions form. On the other hand, similar sulfide inclusions are not thermodynamically stable in the liquid over these composition ranges, and all available sulfur remains in liquid solution.

Using the calculated activity values for each alloy mixture, the corresponding surface tension of the liquid alloys can then be determined as a function of temperature, as shown in Fig. 7 (a). At lower 800H levels, the calculated surface tensions are also significantly lower, particularly in the 10% 800H mixture, than those observed at higher levels of 800H. These differences are directly related to the calculated activity values and the interactions between deoxidizers such as Ti and Al and oxygen. The importance of the role of the minor alloying elements on the surface tension can be further evaluated by comparing these surface tension calculations with those based on ideal solutions, in which the alloying element interactions are ignored. As shown in Fig. 7 (b), the shapes of the curves for each mixture are nearly identical, since the effects of surface-active elements are unchanged with regards to the chemical composition and changes in surface tension are attributed only to the role of the major alloying elements.

The temperature coefficient of surface tension ($d\gamma/dT$) can be extracted from the slopes of the curves in Fig. 7 (a) and (b) to obtain the direction and magnitude of convection. In Fig. 7 (c) and (d), these values are plotted as a function of temperature for the range of FGM compositions considering the interactions between alloying elements and an ideal solution, respectively. Across the range of compositions, $d\gamma/dT$ is positive near the liquidus temperature and becomes more negative as temperature increases. When an ideal solution is assumed and interactions between alloying elements are ignored, insignificant differences in $d\gamma/dT$ are observed over the range of alloy compositions, as shown in Fig. 7 (d). On

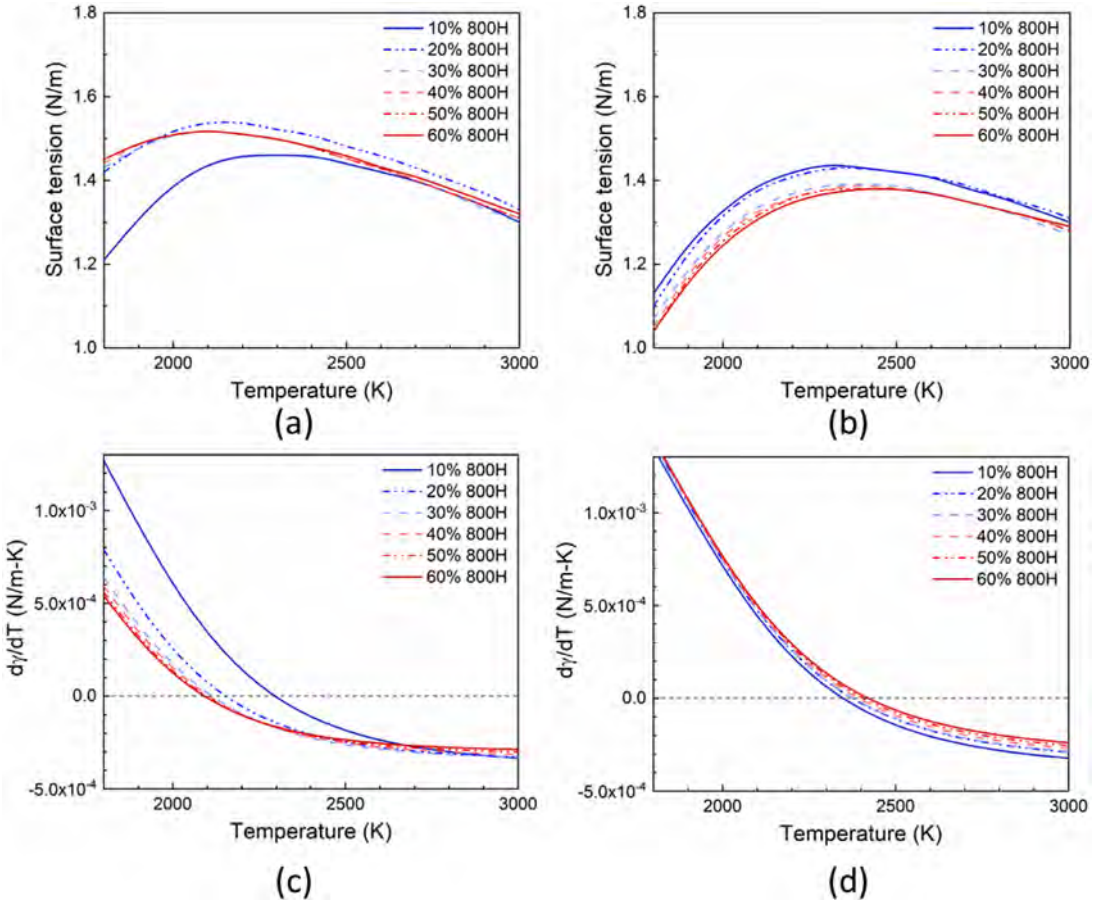

Fig. 7. The calculated temperature dependence of the surface tension (a) considering the interaction between alloying elements and (b) for an ideal liquid solution. The temperature coefficient of surface tension (c) considering the interaction between alloying elements and (d) for an ideal liquid solution.

the other hand, significant differences in the $d\gamma/dT$ values are evident with changes in the FGM compositions, as shown in Fig. 7 (c), when interactions between alloying elements are taken into account.

All $d\gamma/dT$ values calculated across the range of alloy mixtures also display a transition from positive to negative values at temperatures between approximately 2027-2327 K (2300-2600°C). The temperature at which this transition from a positive to a negative value is considered the critical temperature (T_{crit}). In physical terms, T_{crit} represents the temperature at which the liquid metal flow on the surface of a molten pool reverses from an outward to an inward direction, leading to changes in the deposit shape. Changes in the 800H addition for the different FGM compositions have a clear impact on the calculated T_{crit} values. This is shown in Fig. 8, where the highest critical temperatures were observed at low levels of 800H additions and continuously decrease as more 800H is added to the FGM mixture. A higher the value of T_{crit} generally indicates that inward flow will be more pronounced due to a larger region of the molten pool surface having a positive $d\gamma/dT$. However, because the temperatures in the molten pool are determined by process parameters such as laser power, the direction of fluid flow is not solely dependent on T_{crit}. The connection between T_{crit} and fluid flow is discussed further in the next section.

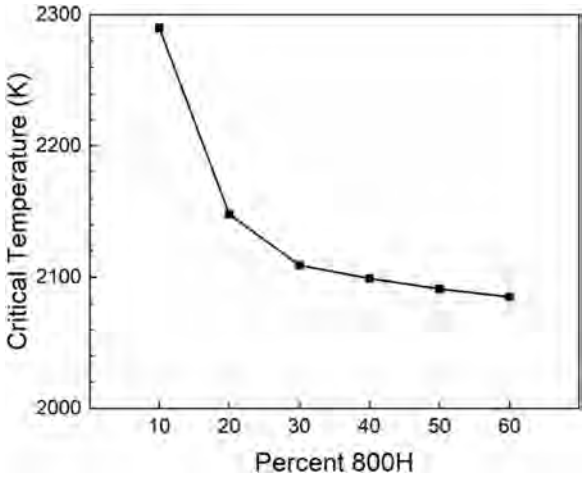

Fig. 8. The critical temperature, defined as the temperature at which the temperature coefficient of surface tension changes from positive to negative, decreases with increasing Alloy 800H additions.

3.3. Molten pool geometry

Changes in alloy composition characteristic of the grading used in the FGM have an impact on both the oxygen and sulfur activity and the resulting surface tension of the liquid metals because all elements in an alloy affect the activity of elements. In order to correlate these changes with the resulting bead shape and size, heat transfer and fluid flow simulations of the AM process [9, 10, 27] were performed. The impacts of changes in the composition on the calculated deposit shapes and sizes considering the oxygen

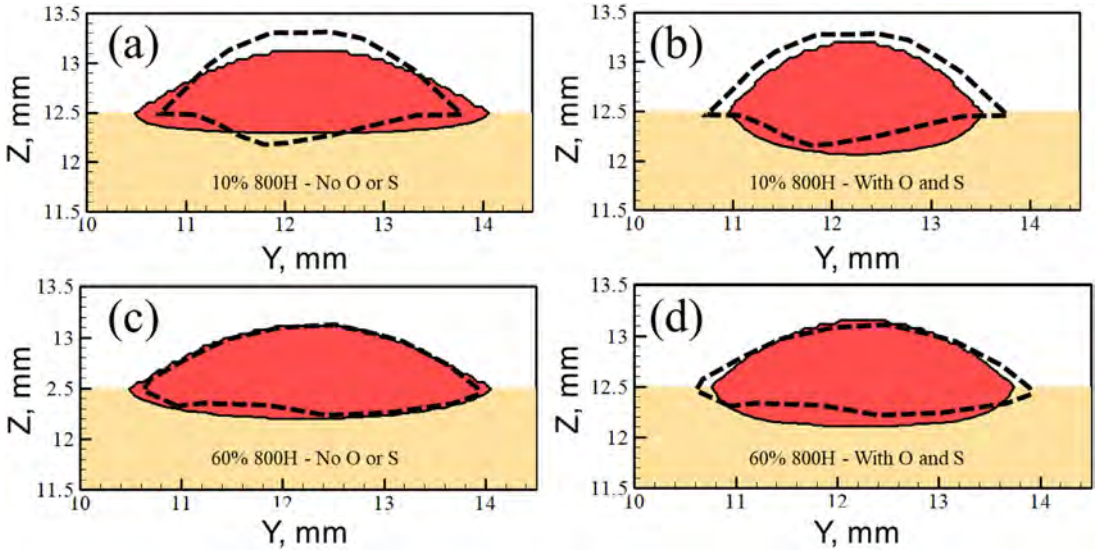

Fig. 9. Comparison of effect of oxygen and sulfur addition on simulated transverse cross-section bead shapes deposited with 2000 W, 10.6 mm/s scanning speed, and 15 g/min powder flow rate. (a-b) 10 % 800H alloy: a) with no oxygen and sulfur content, and b) considering composition with 0.05 wt% oxygen and 0.0151 wt% sulfur in solution, where a_O=0.0082 and a_S=0.0129. (c-d) 60 % 800H alloy: c) with no oxygen and sulfur content, and d) considering composition with 0.05 wt% oxygen and 0.0101 wt% sulfur in solution, where a_O=0.000575 and a_S=0.0086. The black, dashed outlines show the bead shape as measured from the transverse micrograph.

and sulfur activities calculated for each composition are shown in Fig. 9 (a)-(d) for the 10% 800H and 60% 800H additions at a laser power of 2000 W. These compositions are at the extremes of the composition gradient for the FGM joint and encompass the range of oxygen and sulfur activities that will impact the resulting deposit size and shape.

From the comparison of the simulated bead shapes with those obtained experimentally, as shown in Fig. 9 (a) through (d), the changes in composition from 10% 800H to 60% 800H have a significant impact on bead shape and size. In the case of the 10% 800H addition, the simulated deposit shapes, as shown in Fig. 9 (a) and (b), vary when surface-active elements are considered. In particular, the inclusion of oxygen and sulfur activity in the calculations of surface tension reduced the simulated deposit width by 23%, increased the height by 15%, and, most prominently, increased the penetration depth by 115%. With the 60% 800H addition, shown in Fig. 9 (c) and (d), the oxygen activity is lowered and has a decreased impact on the simulated deposit geometry, with the width being reduced by only 14%, the height by 9%, and the penetration depth by 25%.

Overall, when surface-active elements are not considered, the simulated shapes of the 10% and 60% 800H deposits were nearly identical, indicating that the slight changes in thermophysical properties as a function of composition play a negligible role in the experimentally observed deposit shapes. In contrast, the inclusion of oxygen and sulfur in the model produced significantly different molten pool shapes for the two alloys. For 10% 800H, the molten pool shape produced a better match with the experimental results when surface-active elements were considered, with errors of the simulation relative to the experiment being -19%, -14% and +21% for the width, height, and depth, respectively. The results for 60% 800H both with and without surface-active elements matched well with the experimental results, with errors of the simulation relative to the experiment being -14%, -3% and +32% for the width, height, and depth, respectively. The lower width and larger depth of with surface-active elements compared to experiments indicates that the thermodynamic model may have even over predicted the oxygen and/or sulfur activity for those composition. These results indicate the amount of oxygen in solution drives the observed changes in deposit geometries.

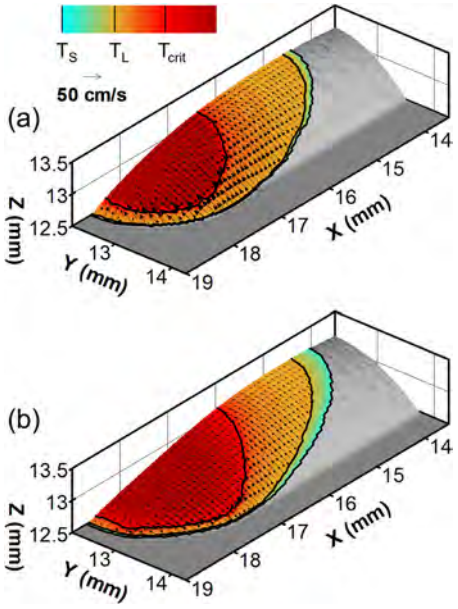

Fig. 10. Three-dimensional views of the surface of the simulated molten pools and deposit geometry for process parameters of 2000 W, 10.6 mm/s scanning speed, and 15 g/min powder flow rate using (a) 10 % 800H and (b) 60 % 800H. Both consider surface-active elements. Contours show the solidus (T_S), liquidus (T_L) and critical (T_{crit}) temperature. Vector represent velocity, the magnitude of which can be approximated using the provided reference vector. Only half of the pool is shown for readability of velocity vectors.

Moving beyond the deposit cross sections, three-dimensional calculations on the deposit surface provide more insight into the fluid flow patterns driving the deposit shape. The impact of increasing 800H additions from 10% to 60% on the fluid flow patterns on the surface of the deposits is shown in Fig. 10 including oxygen and sulfur activities. For example, fluid flow, which is illustrated by the vectors included in each figure, takes an inward direction at temperatures below T_{crit}. With its higher critical temperature, the 10% 800H deposit, shown in Fig. 10 (a), exhibits a larger region of inward fluid flow and larger inward velocities on the deposit sur-

face. The combination of these inward flow characteristics limits the amount of heat transfer to the edge of the pool, thus reducing the deposit width and increasing the depth as heat is concentrated at the center of the molten pool. On the other hand, the increase in the 800H addition shown in Fig. 10 (b) for a 60% 800H addition, produces a different flow pattern, with the fluid flow directed in a mostly outward direction, thus producing a wider and shallower deposit shape.

Many of the trends observed from the simulations in Figs. 9 and 10 can be understood from the impact of surface tension on the shape of the AM fusion zones. The negative value of the temperature coefficient for the pure alloys indicates that fluid will flow from the center of the pool, which is characterized by high temperatures and low surface tension, to the edge of the deposit, where the temperatures are lower and the surface tension is high. The resulting fluid flow leads to enhanced radial heat transfer and produces a wide and shallow molten pool. With the addition of surface-active elements, the temperature coefficient becomes positive below the T_{crit} value, and fluid flow will be reversed and originate at the outer edges of the pool and move towards the middle of the pool. These higher levels of inward flow produce a deposit which is more narrow and deeper than that observed in the absence of these surface-active elements. In both cases shown here, the peak temperature was greater than T_{crit}, but it is theoretically possible to have the peak temperature below T_{crit} to have only inward flow. This could be achieved by process control to lower the peak temperature or by increasing surface-active element activity to raise T_{crit}. However, to consider either approach for process control, alloy composition and the resultant effects on the part properties would have to be assessed.

While the previous calculations have been used to identify the role of oxygen activity on both the surface tension values and deposit size and shape, there is a need to clarify the relative sensitivity of the different alloys to the amount of oxygen present. It is common for oxygen levels to vary between different metal powder sources and to change with processing conditions [20]. To identify how oxygen concentrations can impact deposit shape and size, oxygen contents ranging from 0 to 0.1 wt% O (*i.e.*, 0 to 1000 ppm O) were used to simulate the pool geometry across the range of 800H additions used in the fabrication of the FGM. Results of these simulations for width, height and depth of the deposits are shown in Fig. 11 (a) through (c). The amount of oxygen present in the different alloys, particularly at compositions below 30% 800H additions, can have a significant impact on the deposit geometries. At higher 800H additions, only small variations in deposit geometry are observed because even though a large amount of oxygen is present, the activity of oxygen on the surface remains low because of the presence of Al, Si, or Ti which interacts with oxygen and reduces its concentration and activity in solution. While 0.1 wt% O is higher than any amount of oxygen in the materials used in experiments for this study (0.01 – 0.035 wt% O), this higher level of oxygen was simulated to highlight the difference that oxygen has on the molten pool shape for materials with and without deoxidizing minor alloying elements.

The results presented here directly show the effect of oxygen on pool geometry changes for composition changes in single passes, however, they are indicative of the effects of oxygen as composition throughout an FGM build. As material composition changes throughout the FGM, a corresponding change in fluid flow and pool geometry based on the amount of oxygen in the molten pool will occur, regardless of the layer number. Further, considering the added complexities of boundary conditions in multilayer depositions combined with effects of surface-active elements on molten pool fluid flow and geometry is of interest for future studies. In practical terms regarding the production of FGMs by DED, these results indicate that the use of machine manufacturer's recommended process parameters is not necessarily sufficient to keep the fusion zone shape and size constant and predictable. Furthermore, sensing and control models typically operate on the assumption that fusion zone attributes do not change when the scanning speed, power and other variables are kept constant. This assumption now needs to be reexamined to consider effects of oxygen in each layer of the FGM. Especially in alloys like 2.25Cr-1Mo steel that readily dissolve oxygen in the molten pool, oxygen concentration of the shielding gas and other potential sources of oxygen in the material need to be controlled carefully to achieve repeatable results.

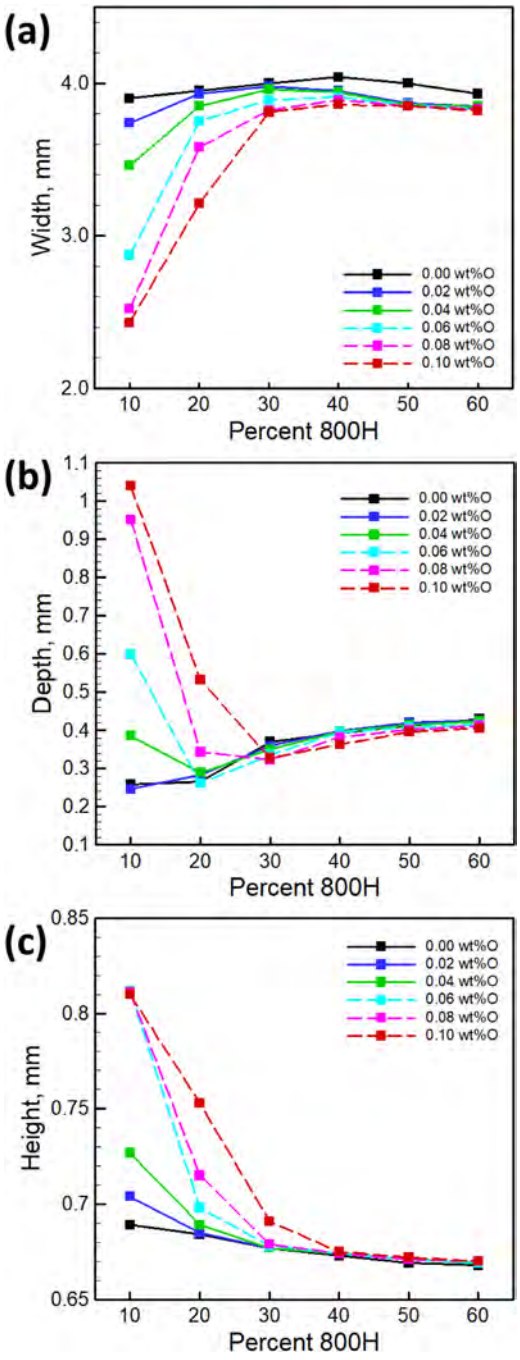

Fig. 11. Simulated variation in pool (a) width, (b) height, and (c) depth as a function of oxygen content and 800H content for a 2000 W laser power and 10.6 mm/s scanning speed.

4. Summary and conclusions

A combination of experiments and numerical simulations was used to investigate the underlying cause of variations in the molten pool geometry in functionally graded materials between 2.25Cr-1Mo steel and Alloy 800H along the build direction. These changes in deposit geometry were replicated through a series of experiments that represented changes in alloy composition along the build direction. The changes in the alloy composition, particularly of aluminum and titanium along the build direction affected the local oxygen concentration in different layers. Deposits containing low levels of 800H additions had high solubility and activities of oxygen that resulted in relatively deep and narrow molten pools. In contrast, deposits with higher levels of 800H additions had lower oxygen activities, which resulted in wide and shallow pool geometries. The following are the main conclusions.

1 During directed energy deposition of functionally graded materials, the fusion zone geometry and temperature fields changed with alloy composition. The change was attributed mainly to the changes in oxygen concentration in the fusion zone owing to changes in alloy composition for the same oxygen concentration in the build environment.
2 Variations in major alloying elements, which determine thermophysical properties, have negligible effects on the shape and size of the molten pool for the alloy compositions investigated. Surface-active elements, particularly oxygen, was the primary factor in changing the overall deposit geometry. The amounts of oxygen in solution affect the variation of surface tension with temperature and the convective flow during directed energy deposition.
3 For all alloy compositions, the amount of oxygen in solution decreased with increasing amounts of deoxidizing elements, like aluminum, titanium, and silicon. The removal of oxygen from solution reduces its activity, which is caused by interactions between oxygen and deoxidizing elements. Consequently, material with higher amounts of 800H contain lower amounts of oxygen in solution because 800H alloy contains multiple deoxidizing elements.
4 The critical temperature within the molten pool, i.e. the point where the surface tension temperature coefficient changes from positive to negative, increases with higher activities of oxygen for all alloy compositions investigated. A higher critical temperature results in more pronounced molten pool flow inward, which results in a relatively deep and narrow deposit geometry. In this case, the critical temperature is highest for the 10% 800H alloy (2290 K) and lowest for the 60% 800H alloy (2085 K).

Declaration of Competing Interest

The authors declare that they have no known competing financial interests or personal relationships that could have appeared to influence the work reported in this paper.

CRediT authorship contribution statement

J.S. Zuback: Methodology, Investigation, Writing - original draft. **G.L. Knapp:** Methodology, Software, Investigation, Data curation, Writing - original draft. **T.A. Palmer:** Writing - review & editing, Supervision, Project administration, Funding acquisition. **T. DebRoy:** Writing - review & editing, Supervision, Project administration, Funding acquisition.

Acknowledgements

The authors gratefully acknowledge financial support from the Department of Energy Nuclear Energy University Program under grant number DE-NE0008280.

Appendix: Surface tension of multicomponent alloys containing surface active elements

A.1. Thermodynamic calculations

In a multi-component alloy, interactions between alloying elements generally cause the activity of an element to deviate from the behavior of in an ideal liquid. The activity of an element, i, in a multicomponent alloy is expressed as:

$$a_i = \exp\left(\frac{\mu_i - \mu_i^0}{RT}\right) \tag{A1}$$

where μ_i is the chemical potential, μ_i^0 is the reference state of element i, R is the gas constant, and T is temperature. Here, the reference state is arbitrary, and is usually taken to be that of the pure element at standard pressure and temperature. A change of reference state is needed to convert the activity calculated from JMatPro® to values with a 1 wt% reference basis. This was achieved by multiplying the calculated activity by a proportionality factor, F, which is the ratio of the activity values from the two different reference states,

$$F = \frac{a_i}{a_i'} = \frac{1}{a_i'} \tag{A2}$$

where a_i is the activity at $i = 1$ wt% in the 1 wt% reference state, and a_i' is the activity at $i = 1$ wt% in the standard reference state.

The modeling of thermophysical properties involves sequential steps. First, the equilibrium distribution of phases is determined through the minimization of the total Gibbs energy method using thermodynamic excess functions to account for the mixing of elements. The property, P, of interest for each phase is expressed as [39]:

$$P = \sum_i x_i P_i^0 + \sum_i \sum_{j>i} x_i x_j \sum_\nu \Omega_{ij}^\nu \left(x_i - x_j\right)^\nu \tag{A3}$$

where P_i^0 is the property of the phase in the pure element, Ω_{ij}^ν is a binary interaction parameter between elements i and j dependent on the integer ν, and x_i and x_j are the mole fractions of i and j in the phase, respectively. The effects of temperature on the property of a phase are accounted for through both P_i^0 and Ω_{ij}^ν, which are temperature dependent. The total property of the alloy is then determined from the phase fractions and properties of each phase using the general law of mixtures [40]. The use of this type of model allows for the approximation of thermophysical properties as functions of composition and temperature and accounts for effects of multi-phase microstructures.

A.2. Calculation of multi-component alloy surface tension

Li et al. [41] demonstrated that generally weak interactions between surface-active elements allows effects of multiple surface-active elements to be additive when considering oxygen and sulfur in an Fe-Cr alloy. Combining this with the temperature-dependent surface tension derived by Sahoo et al. [14], the surface tension can be written generally as,

$$\gamma^P - \gamma = \sum_i^N RT\Gamma_i^0 \ln\left(1 + K_i a_i\right) \tag{A4}$$

The surface tension of the pure metal is γ^P and γ is the surface tension of a binary mixture of the pure metal with element i, both at temperature T. The activity of element i in the mixture is a_i and the surface segregation (i.e., adsorption) at full coverage is given by Γ_i^0. K_i is the adsorption coefficient and R is the universal gas constant. The adsorption coefficient is defined by [14, 33],

$$K_i = k_i \exp\left(-\Delta H_i^\circ / RT\right) \tag{A5}$$

The entropy component of K_i is included by k_i, a constant related to the entropy of segregation, and enthalpy component is included by ΔH_i°, the enthalpy of segregation.

Differentiating Eq. A4 with respect to T gives the temperature coefficient of surface tension,

$$\frac{\partial \gamma}{\partial T} = \frac{\partial \gamma^P}{\partial T} - \sum_i^N \left[R\Gamma_i^0 \ln\left(1 + K_i a_i\right) + \frac{K_i a_i}{\left(K_i a_i + 1\right)} \frac{\Delta H_i^0 \Gamma_i^0}{T} \right] \tag{A6}$$

which is one of the main factors that determines the magnitude and direction of fluid flow during DED-L. The values of ΔH_i°, k_i and Γ_i^0 for the Fe-O system compiled by Sahoo et al. [14] were used for the calculation of surface tension of both 2.25Cr-1Mo steel and 800H alloy containing O since the measured values are not available.

References

[1] C. Zhang, F. Chen, Z. Huang, M. Jia, G. Chen, Y. Ye, Y. Lin, W. Liu, B. Chen, Q. Shen, Additive manufacturing of functionally graded materials: a review, Mater. Sci.Eng.: A 764 (2019) 138209.

[2] A. Bandyopadhyay, B. Heer, Additive manufacturing of multi-material structures, Mater. Sci. Eng.: R: Rep. 129 (2018) 1–16.

[3] G.H. Loh, E. Pei, D. Harrison, M.D. Monzon, An overview of functionally graded additive manufacturing, Addit. Manufactur. 23 (2018) 34–44.

[4] J.S. Zuback, T.A. Palmer, T. DebRoy, Additive manufacturing of functionally graded transition joints between ferritic and austenitic alloys, J. Alloys Comp. 770 (2019) 995–1003.

[5] T. DebRoy, T. Mukherjee, J.O. Milewski, J.W. Elmer, B. Ribic, J.J. Blecher, W. Zhang, Scientific, technological and economic issues in metal printing and their solutions, Nat. Mater. 18 (10) (2019) 1026–1032.

[6] T. Mukherjee, T. DebRoy, A digital twin for rapid qualification of 3D printed metallic components, Appl. Mater. Today 14 (2019) 59–65.

[7] X. Qi, G. Chen, Y. Li, X. Cheng, C. Li, Applying neural-network-based machine learning to additive manufacturing: Current applications, challenges, and future perspectives, Engineering 5 (4) (2019) 721–729.

[8] T. DebRoy, H.L. Wei, J.S. Zuback, T. Mukherjee, J.W. Elmer, J.O. Milewski, A.M. Beese, A. Wilson-Heid, A. De, W. Zhang, Additive manufacturing of metallic components–process, structure and properties, Progress Mater. Sci. 92 (2018) 112–224.

[9] V. Manvatkar, A. De, T. DebRoy, Heat transfer and material flow during laser assisted multi-layer additive manufacturing, J. Appl. Phys. 116 (2014) 124905.

[10] V. Manvatkar, A. De, T. DebRoy, Spatial variation of melt pool geometry, peak temperature and solidification parameters during laser assisted additive manufacturing process, Mater. Sci. Technol. 31 (2015) 924–930.

[11] W. Pitscheneder, T. DebRoy, K. Mundra, R. Ebner, Role of sulfur and processing variables on the temporal evolution of weld pool geometry during multikilowatt laser beam welding of steels, Weld. J. 75 (3) (1996) 71s–80s.

[12] T. DebRoy, S. David, Physical processes in fusion welding, Rev. Mod. Phys. 67 (1) (1995) 85–112.

[13] S.A. David, T. DebRoy, Current issues and problems in welding science, Science 257 (1992) 497–502.

[14] P. Sahoo, T. Debroy, M.J. McNallan, Surface tension of binary metal—surface active solute systems under conditions relevant to welding metallurgy, Metall. Trans. B 19 (3) (1988) 483–491.

[15] Z. Gan, G. Yu, X. He, S. Li, Surface-active element transport and its effect on liquid metal flow in laser-assisted additive manufacturing, Int. Commun. Heat Mass Transf. 86 (2017) 206–214.

[16] M.J. Bermingham, S.D. McDonald, M.S. Dargusch, Effect of trace lanthanum hexaboride and boron additions on microstructure, tensile properties and anisotropy of Ti-6Al-4V produced by additive manufacturing, Mater. Sci. Eng.: A 719 (2018) 1–11.

[17] Y.S. Lee, D.F. Farson, Surface tension-powered build dimension control in laser additive manufacturing process, Int. J. Adv. Manufactur. Technol. 85 (5) (2016) 1035–1044.

[18] I. Gibson, D. Rosen, B. Stucker, Directed energy deposition processes, in: I. Gibson, D. Rosen, B. Stucker (Eds.), Additive Manufacturing Technologies: 3D Printing, Rapid Prototyping, and Direct Digital Manufacturing, Springer, New York, New York, NY, 2015, pp. 245–268.

[19] C.L.A. Leung, S. Marussi, M. Towrie, R.C. Atwood, P.J. Withers, P.D. Lee, The effect of powder oxidation on defect formation in laser additive manufacturing, Acta Mater. 166 (2019) 294–305.

[20] JW Elmer, G Gibbs, The effect of atmosphere on the composition of wire arc additive manufactured metal components, Sci. Technol. Weld. Join. 24 (5) (2019) 367–374.

[21] M. Khanzadeh, S. Chowdhury, M.A. Tschopp, H.R. Doude, M. Marufuzzaman, L. Bian, In-situ monitoring of melt pool images for porosity prediction in directed energy deposition processes, IISE Transactions 51 (5) (2019) 437–455.

[22] Z. Khayat, T. Palmer, Impact of iron composition on the properties of an additively manufactured solid solution strengthened nickel base alloy, Mater. Sci. Eng.: A 718 (2018) 123–134.

[23] A.D. Iams, J.S. Keist, T.A. Palmer, Formation of austenite in additively manufactured and post-processed duplex stainless steel alloys, Metall. Mater. Trans. A 51 (2) (2020) 982–999.

[24] C.A. Schneider, W.S. Rasband, K.W. Eliceiri, NIH image to imagej: 25 years of image analysis, Nat. Methods 9 (7) (2012) 671.

[25] U.R. Kattner, The thermodynamic modeling of multicomponent phase equilibria, JOM 49 (12) (1997) 14–19.

[26] JMatPro®, Sente software.

[27] G.L. Knapp, T. Mukherjee, J.S. Zuback, H.L. Wei, T.A. Palmer, A. De, T. DebRoy, Building blocks for a digital twin of additive manufacturing, Acta Mater. 135 (2017) 390–399.

[28] M.F. Gouge, J.C. Heigel, P. Michaleris, T.A. Palmer, Modeling forced convection in the thermal simulation of laser cladding processes, Int. J. Adv. Manufactur. Technol. 79 (1) (2015) 307–320.

[29] G.L. Knapp, N. Raghavan, A. Plotkowski, T. DebRoy, Experiments and simulations on solidification microstructure for Inconel 718 in powder bed fusion electron beam additive manufacturing, Addit. Manufactur. 25 (2019) 511–521.

[30] J. Millat, M. Mustafa, M. Ross, W.A. Wakeham, M. Zalaf, The thermal conductivity of argon, carbon dioxide and nitrous oxide, Phys. A: Stat. Mech. Appl. 145 (3) (1987) 461–497.

[31] S. Patankar, Numerical heat transfer and fluid flow, Hemisph. Publish. Corp. (1980).

[32] R. Rai, G.G. Roy, T. DebRoy, A computationally efficient model of convective heat transfer and solidification characteristics during keyhole mode laser welding, J. Appl. Phys. 101 (2007) 054909.

[33] M. J. McNallan and T. DebRoy, Effect of temperature and composition on surface tension of Fe-Ni-Cr alloys containing sulfur, Metall. Trans., B, 1991, 22B (1991) 557-560.

[34] C.S. Wu, L. Dorn, Computer simulation of fluid dynamics and heat transfer in full-penetrated TIG weld pools with surface depression, Comput. Mater. Sci. 2 (2) (1994) 341–349.

[35] A. Kumar, T. DebRoy, Heat transfer and fluid flow during GMA fillet welding for various joint configurations and welding positions, Metall. Mater. Trans. A–Phys. Metall. Mater. 38A (3) (2007) 506–519.

[36] I. Tabernero, A. Lamikiz, E. Ukar, L.N. López de Lacalle, C. Angulo, G. Urbikain, Numerical simulation and experimental validation of powder flux distribution in coaxial laser cladding, J. Mater. Process. Technol. 210 (15) (2010) 2125–2134.

[37] J.C. Haley, J.M. Schoenung, E.J. Lavernia, Observations of particle-melt pool impact events in directed energy deposition, Addit. Manufactur. 22 (2018) 368–374.

[38] S. Mishra, T.J. Lienert, M.Q. Johnson, T. DebRoy, An experimental and theoretical study of gas tungsten arc welding of stainless steel plates with different sulfur concentrations, Acta Mater. 56 (9) (2008) 2133–2146.

[39] Z.-K. Liu, Y. Wang, Computational thermodynamics of materials, Cambridge University Press, Cambridge, UK, 2016.

[40] Z. Fan, P. Tsakiropoulos, A.P. Miodownik, A generalized law of mixtures, J. Mater. Sci. 29 (1) (1994) 141–150.

[41] Z. Li, K. Mukai, M. Zeze, K.C. Mills, Determination of the surface tension of liquid stainless steel, J. Mater. Sci. 40 (9) (2005) 2191–2195.